Nanoscale

PAPER

View Article Online
View Journal

Cite this: DOI: 10.1039/d5nr04824a

Pressure-controlled oxygen activation at single metal atom sites in a manganese–cobalt coordination network on graphene: from triplet–singlet spin transition to superoxo dissociation

Asha Yadav,[a] Stefania Baronio,[b] Michela De Col,[b] Danilo Comini,[b] Valentin Mischke,[c] Alessandro Namar,[b] Nikolay Vinogradov,[d] Mattia Scardamaglia,[d] Mirko Cinchetti,[c] Giovanni Zamborlini,[c,e] Paolo Giannozzi *[a,f] and Erik Vesselli *[b,g,h]

Received 14th November 2025,
Accepted 7th March 2026

DOI: 10.1039/d5nr04824a

rsc.li/nanoscale

Molecular oxygen activation at single transition metal atom sites is critical for catalysis but remains challenging to control. Here we investigate a manganese–cobalt bi-metallic coordination network on graphene, where Co(I) atoms are tetracoordinated by nitrogen. Combining density functional theory with *in situ* infrared-visible sum-frequency generation and ambient-pressure X-ray photoelectron spectroscopy, we demonstrate pressure-dependent oxygen ligation at Co sites. Below 10^{-6} mbar, O_2 binds reversibly in a horizontal configuration, inducing charge transfer and a triplet-to-singlet spin transition characteristic of an active superoxo $O_2^{\delta-}$ species. Increasing oxygen pressure leads to O_2 dissociation, with atomic oxygen accumulating at Co(II) sites and at the support. Co-exposure to O_2 and CO enables room-temperature oxidation of the latter, preventing catalyst poisoning. These findings reveal how coordination and environmental control tune spin, oxidation state, and reactivity at single metal atoms, offering pathways for rational design of atomically precise two-dimensional catalysts.

1 Introduction

Oxygen–oxygen bond formation and cleavage are fundamental elementary reaction steps involved, for example, in the oxygen evolution and reduction reactions (OER and ORR, respectively), which are of great technological importance in the field of renewable energy schemes. The search for efficient catalytic materials with multifunctional properties, high selectivity and activity, associated with low-cost raw materials, is intensely pursued. In this regard, the design of novel materials based on fundamental principles, yielding emergent physical and chemical properties originating from the complex interplay between building blocks, constitutes an interesting premise. A novel approach in this sense consists in the bottom-up assembly of bio-mimetic materials, and we focus here on the growth of surface-confined 2D metal–organic coordination networks. Specifically, metalloporphyrins can be exploited as molecular tectons with tuneable catalytic activity, magnetic, and storage properties.[1–8] Metalloporphyrins feature an extensive delocalized π-system that can be tailored by means of peripheral residues and an unsaturated core part that can stabilize a large variety of single metal ions, thus offering tuning opportunity of the optical, chemical, magnetic, and electronic properties.[9] In addition, both lateral interactions and the surface *trans* effect (fifth ligand)[10] can be exploited to further tune the features of the tectons, as well as the self-assembly into 2D ordered superstructures at surfaces or 2D materials heterostacks.[11,12] The catalytic activity of the single metal ions coordinated in the porphyrins' macrocycle or in similar tectons, like *e.g.* phthalocyanines, has been extensively addressed, also specifically toward the OER, ORR, and the carbon dioxide reduction reaction (CO_2RR).[13–17] By taking advantage of the structural flexibility of metalloporphyrins and by exploiting metal coordination at the peripheral moieties, the fabrication of a supramolecular metal–organic coordi-

[a]*Department of Mathematics, Computer Science, and Physics, University of Udine, 33100 Udine, Italy. E-mail: paolo.giannozzi@uniud.it*
[b]*Department of Physics, University of Trieste, via A. Valerio 2, 34127 Trieste, Italy. E-mail: evesselli@units.it*
[c]*Department of Physics, TU Dortmund University, 44227 Dortmund, Germany*
[d]*MAX IV Laboratory, Lund University, 22100 Lund, Sweden*
[e]*Institute of Physics, NAWI Graz, University of Graz, Universitätsplatz 5, 8010 Graz, Austria*
[f]*CNR – Istituto Officina dei Materiali (IOM), SISSA, 34136 Trieste, Italy*
[g]*CNR – Istituto Officina dei Materiali (IOM), S.S. 14 km 163.5, Area Science Park, 34149 Basovizza, Trieste, Italy*
[h]*Center for Energy, Environment and Transport Giacomo Ciamician, University of Trieste, 34127 Trieste, Italy*

nation network with alternating Cu(0) and Cu(II) centres occupying two different chemical environments was obtained.[18] This approach was further extended both theoretically and experimentally towards bimetallic networks of *meso*-substituted M_1TPyP-M_2 porphyrins with M_1 = Co, Fe; M_2 = *, Co, Fe, yielding 2D assemblies with emergent electronic and magnetic properties and outstanding ORR performance (* = empty site).[15,19,20] These networks tend to form long-range ordered superstructures, which contain single Co atoms tetra-coordinated by nitrogen with tuneable oxidation state in the +1 to +3 range, in close resemblance with the vitamin B12 properties.[21,22] Tuning of the Co oxidation state allowed for the selective ligation of CO – Co(I) sites – or activation of O_2 – Co(II) sites.[23–25] Recently, we successfully synthetized and characterized in UHV (ultra-high vacuum) conditions a similar system, based on Mn–Co single metal atom centres supported on quasi free-standing graphene (Gr).[26] We focus here on the reactivity of the layer with respect to oxygen ligation and activation. Monometallic Mn porphyrin complexes have been extensively studied in various forms with different oxidation states for both O_2 activation and nitrosyl adduct formation.[27,28] In this case, the influence of Co coordination to the *meso*-substituents remains unexplored for tetra-pyridyl porphyrins. Given that Mn is a third-row transition metal adjacent to Fe and Co in the periodic table, further investigation is expected to provide deeper insight into the fundamental properties governing the active site behaviour. Referring to the pioneering experimental work on the M_1TPyP-M_2 networks,[15,19,20] the effect of the insertion of the second (M_2 = Co) peripheral metal in addition to the macrocycle metal atom (M_1 = Fe) is very evident towards OER. Interestingly, the activity is found to be much higher compared to the opposite case of M_2 = Fe added to a CoTPyP macrocycle (M_1 = Co). The effect of switching the $M_{1,2}$ = Fe, Co positions is puzzling, given that both elements have a nominal +2 oxidation state in both chemical environments. The goal of our investigation is thus to explore how the metal interchange affects the electronic structure and, in turn, O_2 reactivity when switching to M_2 = Mn.

In this combined theoretical and experimental study, we address how the presence of Co adatoms at the periphery of MnTPyP molecules on graphene influences the activation and dissociation of O_2. Using density functional theory, we show that while Mn centres weakly bind O_2 without inducing significant activation or spin transitions, Co centres exhibit strong O_2 adsorption with substantial charge transfer, O–O bond elongation, and a spin transition from triplet to singlet – hallmarks of an activated superoxo state. Infrared-visible sum-frequency generation (IR-Vis SFG) spectroscopy and ambient-pressure X-ray photoelectron spectroscopy (AP-XPS) confirm that O_2 ligation is pressure-dependent and localized at the Co sites. At low pressure, ligation is reversible, while at higher pressures, O_2 dissociates, leading to irreversible oxidation of the Co centres and of the graphene substrate. Exposure of the layer to both O_2 and CO demonstrates that reactive atomic oxygen species can be removed *via* room-temperature oxidation of CO, offering a strategy to mitigate surface poisoning. These results reveal how design and tuning enable control over molecular oxygen activation and dissociation at the single-atom level in an engineered functional 2D material.

2 Results and discussion

2.1 Computational description of the O_2 interaction with the monometallic MnTPyP layer on graphene

To investigate O_2 ligation at the single metal atom sites of the layer, DFT structural optimizations were performed, starting from the optimized monolayer structure yielding the calculated density of states (Fig. 1a and c for the MnTPyP/Gr case) already reported in our previous study.[26] The O_2 molecule, with a starting, contracted bond length of 1.16 Å, was initially placed in both vertical (V-conf) and horizontal orientations (H-conf) at a distance of 2 Å above the selected metal atom (see Fig. S1 for the similar MnTPyP-Co case). For the monometallic MnTPyP/Gr structure, Fig. 2a, b, d and e displays the optimized geometries when starting from the H-conf (a and b) and V-conf (d and e) of the O_2 molecule, respectively, above the Mn site. Terminal ("end-on") O_2 in V-conf is found to be the most favourable configuration (E_{ads} = 0.71 eV), being more stable by 0.28 eV with respect to the bridge ("side-on") H-conf geometry (E_{ads} = 0.43 eV). The molecular axis defines a bonding angle of 61° (Mn–O–O) with respect to the surface normal. The results translate into a mild covalent bonding for O_2 ligation at the Mn site of the MnTPyP/Gr layer. Generally, PBE calculations work well for chemisorption but are known to overestimate the binding energy.[29] In addition to the adsorption energy, the intramolecular O_2 bond length is another descriptor of the interaction nature and strength. In this case, ligation to Mn mildly lengthens the O–O bond from 1.22 (calculated gas phase value) to 1.27 Å (+4%). Generally, the larger the bond length, the more favourable the dissociation, indicating, in this case, poor activation of the molecule. It is also well-known that oxygen binding to the single metal atom sites of porphyrins induces spin state changes, which are closely related to activation and dissociation. A free oxygen molecule exhibits triplet states with two unpaired electrons contributing to the magnetic moment of $2\mu_B$ in the ground state.[30] A transition from triplet to singlet state configurations in O_2 is known to accompany activation. This phenomenon is well documented in the literature, especially for iron porphyrins coordinated with histidine, imidazole, and related ligands.[31,32] Nevertheless, in this case, no crossover of spin state was found. Also, Mn remains in the pristine high-spin state with a minor change in the occupancy, resulting in a Mn oxidation state slightly higher than +2. The projected density of states was analysed in Fig. S2, where components of the Mn 3d and O 2p orbitals before and after O_2 ligation are plotted. Although a small amount of rearrangement of the density of states near the Fermi level can be seen, no significant orbital hybridization between Mn 3d and O 2p can be observed, confirming a weak interaction. This is also sup-

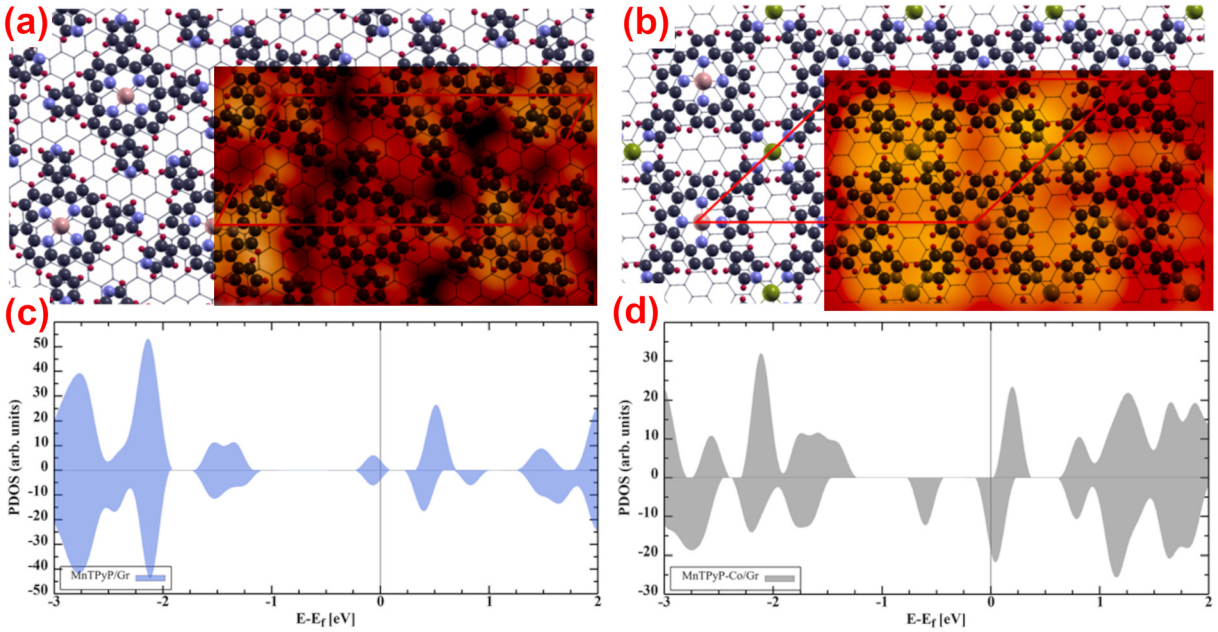

Fig. 1 Geometrically optimized (a) monometallic MnTPyP/Gr and (b) bimetallic MnTPyP-Co/Gr monolayers structures superimposed on the corresponding experimental STM images, together with the respective spin-resolved total density of states (c and d). Gray, blue, light orange, light red, and green spheres represent C, N, Mn, H, and Co atoms, respectively.

ported by the charge density difference plot and Bader charge analysis (Fig. 2c and f), which indicates a small ($0.13e^-$) charge shift to the proximal oxygen atom. This could be attributed to the highly stable high-spin state of Mn 3d, hindering the Mn–O_2 interaction. Compared to the Fe porphyrin case,[33] the weaker Mn–O bond formation, attributed to the high spin state, is directly associated with a higher O_2 dissociation barrier. Thus, although the adsorption process is found to be mildly exothermic, we can conclude that O_2 bonding at the Mn site is quite unstable at room temperature.

Our experiments confirm the theoretical picture. IR-Vis SFG spectroscopy measurements of the MnTPyP/Gr/Ir(111) layer at room temperature from UHV up to 1 mbar did not reveal any evidence of O_2 ligation, nor dissociation, with all vibronic features remaining unaltered upon exposure to oxygen.

2.2 Computational description of the O_2 interaction with the bimetallic MnTPyP-Co layer on graphene

Upon post-addition of Co adatoms, as depicted in Fig. 1b, the latter bind to the peripheral terminal pyridinic sites, inducing a structural re-arrangement of the layer so that tetra-coordination with N atoms is achieved. A bimetallic MnTPyP-Co/Gr layer is thus formed, with a square unit cell, two non-equivalent, potentially active single metal sites, Mn and Co, and significant changes in terms of electronic structure (Fig. 1c and d), work function, and magnetic properties with respect to the pristine MnTPyP/Gr layer.[26] These two single-atom sites were probed towards O_2 ligation, again starting from both V-conf and H-conf. It was found that at the Mn site both geometrically optimized configurations converge to a similar and close to degenerate O_2 adsorption geometry (E_{ads} = 0.91–0.92 eV) as shown in Fig. 3a and b. The O_2 molecule reorients upon structural relaxation, adopting an oblique configuration with an angle of approximately 63° (M–O–O) relative to the surface normal. This angle is close to the Mn–O–O bond angle found in the case of O_2 ligation at the Mn sites of the monometallic MnTPyP/Gr layer. The O_2 adsorption energy increases by almost 30% compared to the case of the latter monometallic layer. This is supported by the Bader charge analysis, indicating a charge transfer of $0.2e^-$ from the metal to the closest O atom, resulting in a slightly reduced Mn–O bond length (2.18 Å compared to 2.20 Å) and in an intramolecular O_2 bond further increased to 1.28 Å, in agreement with the general accepted rule of a correlation between binding energies and O=O double bond lengthening (weakening).[34] Thus, while we can conclude that the presence of peripheral metal ions (Co) affects the properties of the metal ion in the macrocycle, DFT calculations show that, still, Mn and O_2 persist in their high-spin state, being this a strong indication that activation (O_2 dissociation) is unlikely.

Significantly larger adsorption energy values are obtained for O_2 ligation at the Co site of the bimetallic layer. For the H-conf (Fig. 3c and d) and V-conf (Fig. 3e and f) orientations, values of 1.34 and 1.23 eV are obtained, respectively. This indicates a stronger binding and suggests that formation of the Co–O–O bond could be observed experimentally at room temperature as well. Similarly to the Mn site, the "end-on" (vertical, V-conf) configuration is characterized by an oblique molecular axis, bent by 41°, and an intramolecular bond length of 1.27 Å. The latter quantity further increases in the horizontal, most

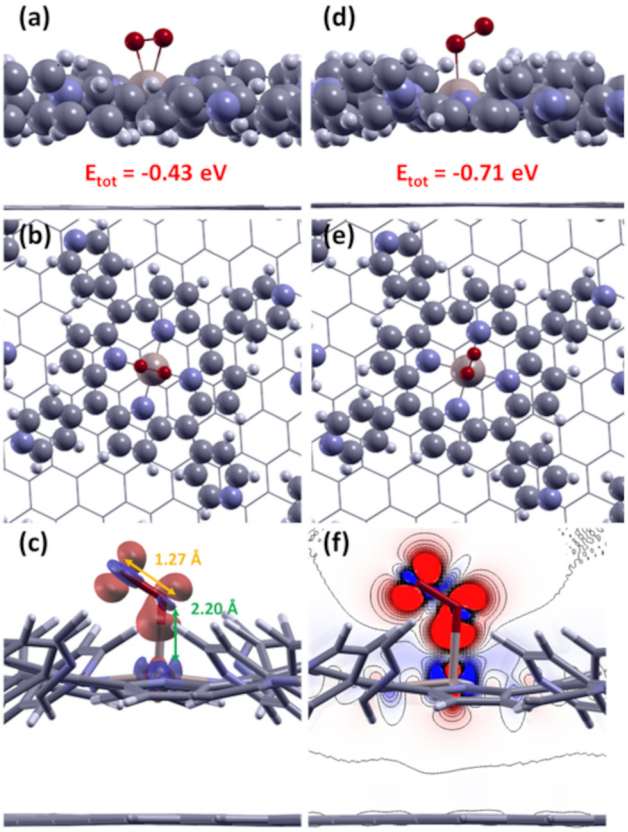

Fig. 2 Top and side views of the optimized O_2 molecule ligated at the Mn site of the monometallic MnTPyP/Gr layer after starting relaxation from the two different configurations: (a and b) H-conf and (d and e) V-conf, with the former yielding a metastable configuration and the latter the lowest energy geometry; for the best structure, side views of (c) the volumetric charge density difference plot and (f) the corresponding 2D charge density difference distribution (0.005e^- isovalue) along the plane passing through the Mn atom and perpendicular to the plane of the Gr sheet. Gray, blue, light orange, and light gray represent C, N, Mn, and H atoms, respectively.

stable bonding geometry, reaching 1.32 Å, compatibly with O_2 dissociation. Consistently, a significant charge redistribution between O_2 and the MnTPyP-Co/Gr layer is observed (Fig. 4). The Bader analysis quantifies a net charge transfer of 0.19 and 0.21e^- to the O atoms in the oxygen molecule, with an overall 0.4e^- doping in the direction of a superoxo species ($O_2^{\delta-}$ with δ = 0.4), yielding a significant weakening of the intramolecular bond, a prerequisite for dissociation. This is a widely accepted characteristic of the horizontal adsorption geometry.[33] O_2 ligation shifts the Co oxidation state from +1 to +2 and, most interestingly, induces a spin transition of the O_2 molecule from the triplet to the singlet state. Summarizing, O_2 adsorption at the Co sites of the bimetallic layer is found to yield the most stable ligation configuration in the horizontal geometry. Our calculations also provide indirect evidence (the values of bond lengths, charge transfer, metal oxidation state, and spin configuration) for Co single metal atom sites of the MnTPyP-Co/Gr layer being reactive towards O_2 ligation, activation and dissociation at room temperature. To verify that the improved Co–O_2 interaction is a site-dependent process, Co–O_2 adsorption on CoTPyP-Mn/Gr was also examined, with particular emphasis on the Co occupying the core site, as detailed in the SI. Our results show that Co occupation at the core and peripheral sites leads to a significantly different metal–O_2 interaction.

In order to better assess the character of the ligation, we computed the potential energy profiles along the ligation pathways for the horizontal O_2 configuration at both the Co and Mn sites of the bimetallic layer (Fig. S3). We find that O_2 ligation is activated, with a much larger barrier for the Mn site (0.52 eV, red profile) compared to the Co site (blue profile), where the barrier is almost negligible for a room temperature gas (0.08 eV). We also mention that the final configurations of our reaction paths are the metastable geometries, which are potential precursors to dissociation. A subsequent dissociation step might follow the same pattern of O_2 dissociation at the metal site of a porphyrin:[33] one of the two O atoms binds to the metal atom, while the other attaches to the closest C–C bond of the macrocycle, as the π bond is energetically favourable.

2.3 Low-pressure experiments

Our experimental results provide solid confirmation for our theoretical findings. The reactivity towards molecular oxygen of the MnTPyP-Co/Gr/Ir(111) system was first investigated by means of *in situ* IR-Vis SFG spectroscopy. We observed an evolution of the coordination network spectra upon exposure to O_2, associated with the interaction between the layer and the gas phase. Even if we were unable to resolve experimentally the specific ν(O–O) mode associated with the internal stretching motion of adsorbed oxygen, we could confirm its presence by XPS. This is not a surprising issue, since the vibronic signal amplitude of ligated O_2 depends on its low dipole and can be further damped by a slanted bonding geometry, in agreement with our DFT calculations that predict the horizontal bonding as the most stable configuration. In a low-pressure regime (p_{O_2} < 1 × 10^{-6} mbar) we find that di-oxygen ligation is reversible at room temperature. Fig. 5a reports the spectra collected in ppp polarization combination in the 1200–1330 and 1500–1680 cm^{-1} ranges, respectively, while the second range measured in ssp polarization is depicted in panel (b) of the figure. The lineshape parameters and line positions were fitted globally (*i.e.* the parameters were optimized on the whole data set) and consistently with the parameters obtained by fitting the UHV spectrum of the pristine layer. The assignment of the observed vibronic features, together with a detailed quantitative description of their evolution, is reported in the SI (see Table S1 and text there below). All visible features originate from internal motion modes of the macrocycle or pyridyl moieties, apart from a contribution slightly above 1600 cm^{-1}, which can be associated also with the Gr phonon.[35] In 7 × 10^{-7} mbar O_2, we observe a spectral evolution in both energy ranges and polarizations (central row in Fig. 5). These variations are induced by the interaction with oxygen and can be described

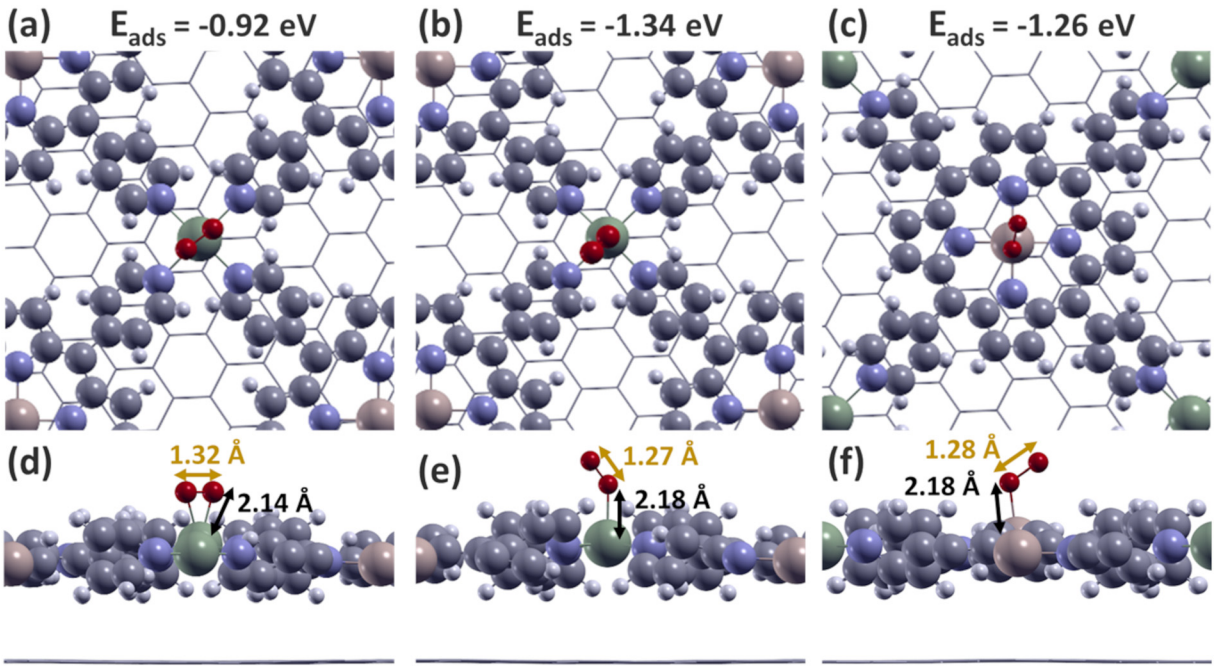

Fig. 3 Top and lateral views (top and bottom rows, respectively) of the most stable structures achieved upon optimization of the O_2 molecule adsorption geometries at Mn (a and b) and Co (c–f) sites of the bimetallic MnTPyP-Co/Gr layer; while in the case of the Mn site the final configuration is close to degenerate when starting from the H-conf or V-conf, a metastable vertical ligation geometry is found at the Co sites (e and f) in addition to the most stable horizontal coordination (c and d). Here, gray, blue, light orange, white, and green spheres represent C, N, Mn, H, and Co atoms, respectively.

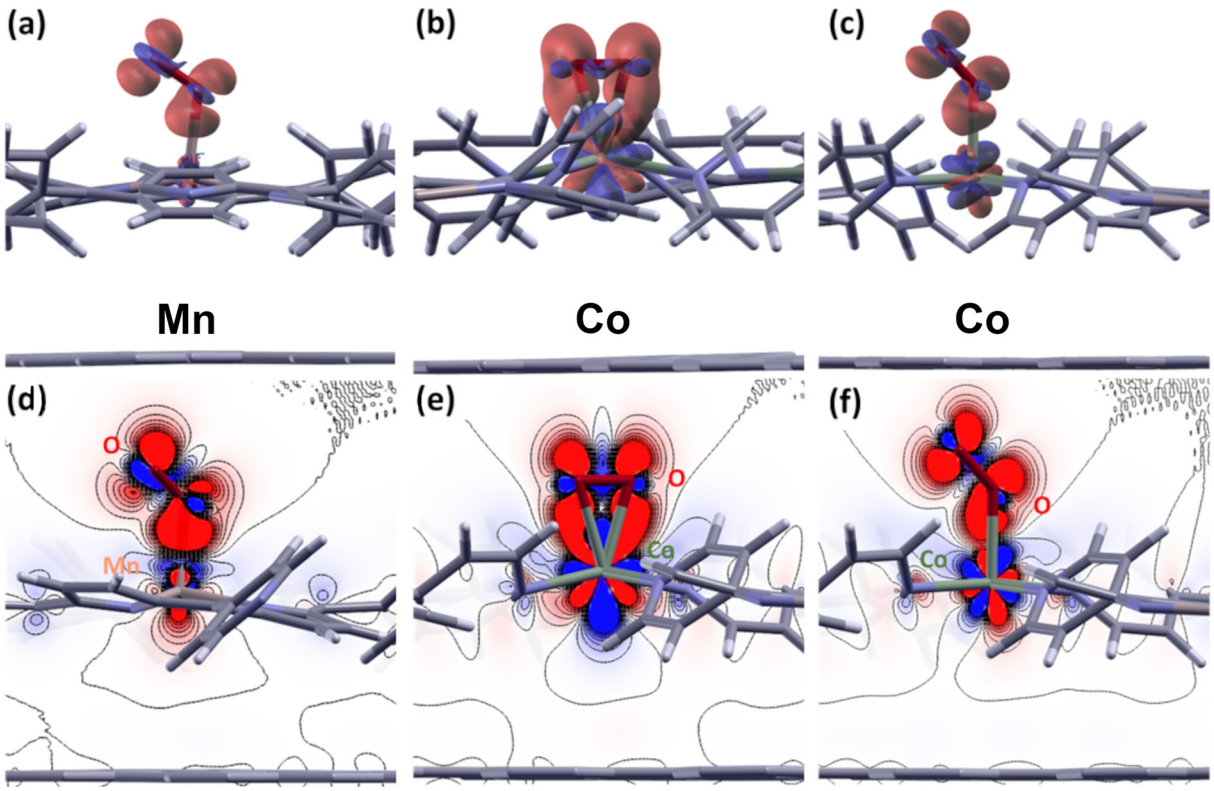

Fig. 4 Side views of the volumetric charge density difference (top row) and of the corresponding 2D charge density difference distribution (bottom row) cut along the plane passing through the Co/Mn atoms and perpendicular to the plane of the Gr sheet ($0.005e^-$ isovalue): Mn site in (a and d) V-conf, Co site in (b and e) H-conf and (c and f) V-conf.

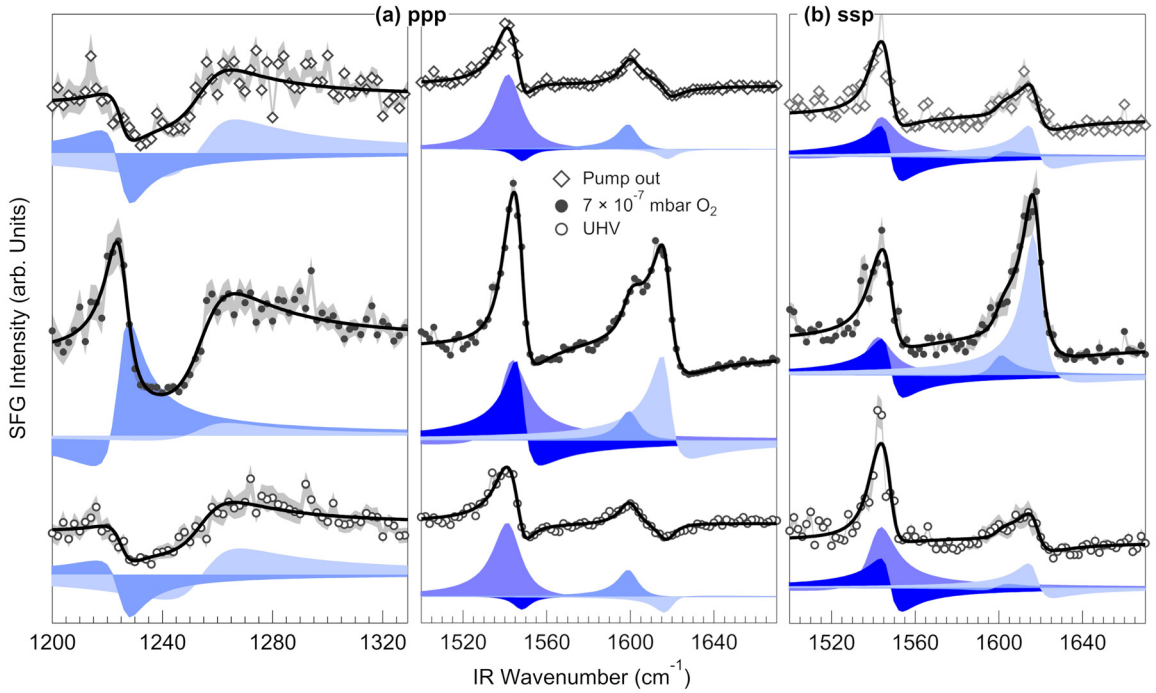

Fig. 5 Sum-frequency generation spectra of the pristine MnTPyP-Co layer in UHV (bottom), in low background oxygen pressure (middle row), and after recovering UHV conditions (top row). All spectra were collected *in situ* and at room temperature with a visible laser wavelength of 532 nm in both (a) ppp and (b) ssp polarization combinations.

by changes in phases and amplitudes associated to the resonances, and to a modified non-resonant background. The reversible nature of this evolution when recovering UHV conditions (Fig. 5, top row) further confirms the weak interaction between the O_2 molecules and the metal–organic network, indicating reversible ligation with no dissociation below this low-pressure threshold. Similarly, reversible O_2 ligation has already been observed on Co-porphyrins.[25,36] According to the experimental picture and in agreement with the theoretical modelling, molecular oxygen ligation induces a deformation of the peripheral rings, with a major involvement of the δ(pyr) modes associated to the N moieties that directly coordinate Co, confirming this latter site as the active metal species in the adsorption process.

The corresponding parallel results obtained by means of AP-XPS are shown in Fig. 6. Starting from UHV (bottom row spectra), we obtain the characteristic spectral deconvolution of (a) Co $2p_{3/2}$ and (b) Mn $2p_{3/2}$ as we previously reported.[26] The first relevant piece of information is that Co is confirmed to be the reactive site, while Mn is not directly involved in the O_2 activation process. In fact, the Mn $2p_{3/2}$ spectrum acquired in O_2 background is well described by the same lineshape of Mn (III)-like species, typical of the pristine MnTPyP-Co/Gr layer.[26] This is in agreement with the experimental study of the reactivity of Mn-porphyrins with respect to O_2,[37] where only Mn(II) was identified as the active species toward oxygen.

In contrast, the Co $2p_{3/2}$ core level is strongly affected upon exposure to O_2. Two new components grow at 781.4 and 783.1 eV at the expense of the intensity of the Co(I) features. We assign these O_2-related peaks to the multiplet splitting features of a new cobalt species interacting with oxygen. The 1.7 eV energy separation between these peaks is close to the value of the multiplet split components of Co(I) in the pristine layer (1.8 eV). However, now, these are shifted by +1.1 eV (excluding the Gunnarsson and Schönhammer – GS – component).[38] According to the previously reported data, the new spectral contributions can be ascribed to a Co(II) species (Table S2). In the form of Co(II)O, this species is modelled with two peaks separated by 2.1 eV,[39] while in a Co(II)TPyP/Gr layer additional features are distinguished at 780.1, 782.1 and 784.3 eV (excluding the GS contribution),[40] and a similar behaviour is observed for CoTPP/Cu upon Co oxidation.[41] In our case, we can separate only two features at intermediate energies between the three components resolved in a Co(II)TPyP monolayer,[40] due to the superposition of Co(II) and Co(I) contributions. In addition, the GS peak of Co(I) is not completely quenched, indicating that not all Co sites are oxidized at this oxygen pressure. The same spectroscopic structure, including both the Co(I) and Co (II) features, is employed to model also the pump out spectrum. Indeed, what we observe is that the GS peak grows back to ~65% of its initial intensity, at the expense of the Co(II) components. However, about 55% of the feature at 781.4 eV stays after the pump out, suggesting that a partially non-reversible oxidation process has already taken place during the long spectra (several hours) acquisition time. Correspondingly, three components are distinguished at 529.7, 531.2 and 532.9 eV in the O 1s core level spectra in Fig. 6c upon exposure to O_2. We resolve a feature that can be associated with molecular

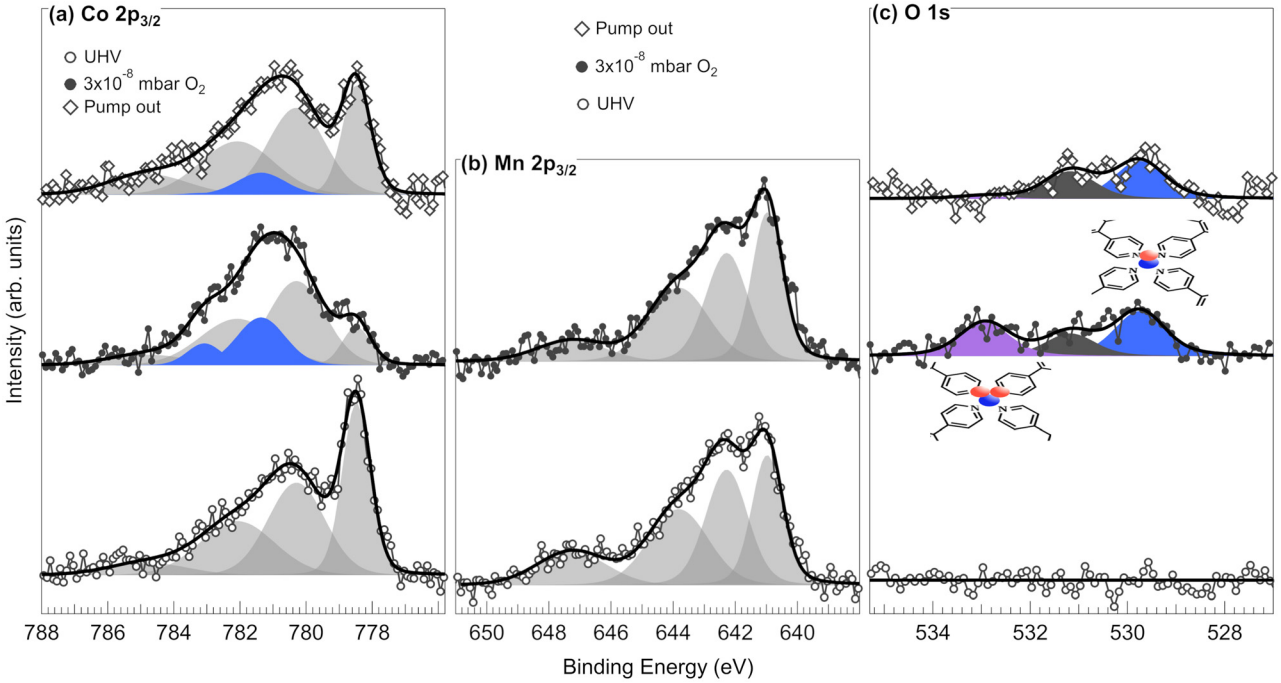

Fig. 6 XPS spectra of the pristine MnTPyP-Co layer in UHV (bottom), in low background oxygen pressure (middle row), and after recovering UHV conditions (top row). (a) Co $2p_{3/2}$ and (b) Mn $2p_{3/2}$ core level regions were collected with a photon energy of 1000 eV, while for (c) the O 1s region photons of 750 eV were chosen for optimal measurement conditions.

oxygen ligated at the Co site, at 532.9 eV, in agreement with both SFG data interpretation and computational predictions. The latter spectroscopic peak is completely quenched when recovering UHV, accounting for the reversible behavior of the Co $2p_{3/2}$ and the IR-Vis SFG spectra. The binding energy of this peak is found in between values associated with molecular oxygen physisorbed and chemisorbed on metals, as reported in Table S2. More specifically, O_2 physisorbed on metals is found at about 535.8–536.9 eV,[42] at approximately 3 eV higher binding energy with respect to our case, at an energy where we observe no photoemission intensity. On the other hand, molecular oxygen strongly chemisorbed in the form of peroxo (O_2^{2-}) or superoxo (O_2^{-}) species is found in the 529.6–530.5 eV range on Pt,[42] 530.9–532.1 eV on Ag,[43] and at 532.1 eV as active O_2^{-} on Co.[44] Thus, we attribute the reversible feature at 532.9 eV to dioxygen chemisorbed on cobalt, where a partial charge transfer to a metastable $O_2^{\delta-}$ species accounts for the peculiar binding energy, which is only 0.8 eV higher than O_2^{-}/Co,[44] well away from the physisorbed O_2 position. The attribution of the remaining O 1s features at 529.7 and 531.2 eV is more challenging due to the overlap of the broad energy ranges where chemisorbed molecular and atomic oxygen species have been observed on metals (Table S2). In our interpretation, both peaks originate from atomic oxygen species, based on their non-reversible character and on the residual Co oxidation observed upon removal of the oxygen background. We associate the species at 529.7 and 531.2 eV with atomic O bound to cobalt and to carbon, respectively. Focusing on the former, similar spectral contributions have been observed on oxidized Gr/Ir(111) and were attributed to enolate and epoxy species (atomic O on Gr with single or double bonds, respectively).[45,46] In our case, the trace amount of oxygen present on the sample after exposure to very low O_2 pressure produces a very weak signal, making it impossible to distinguish such contributions. As we show later in this work, this is not the case for higher oxygen pressures.

Finally, the lowest binding energy component is in good agreement with the energy of CoO in the 529.5–530.2 eV range.[44,47] In the case of vertical (or "end-on") O_2 ligation, the two oxygen atoms within the molecule become non-equivalent, resulting in two distinct contributions to the O 1s core level.[48] This is not the case here, so that we confirm horizontal (or "side-on") adsorption, in close agreement with our theoretical predictions. We have so proven experimentally that the active metal site for O_2 ligation is Co and that, at room temperature and low di-oxygen pressure, the O_2 molecules almost reversibly ligate in the form of activated $O_2^{\delta-}$. Reversible ligation is the precursor to the activation of molecular oxygen, suggested by the residual fingerprint of atomic oxygen on the layer and partially oxidized cobalt. Therefore, this demonstrates that a bimetallic MnTPyP-Co network on Gr/Ir(111) can activate the O_2 intramolecular bond potentially promoting its dissociation at room temperature.

2.4 High pressure experiments

The IR-Vis SFG spectra relative to the high-pressure investigation are presented in Fig. 7, showing the 1200–1290 and 1500–1650 cm^{-1} spectral ranges, collected in ppp polarization.

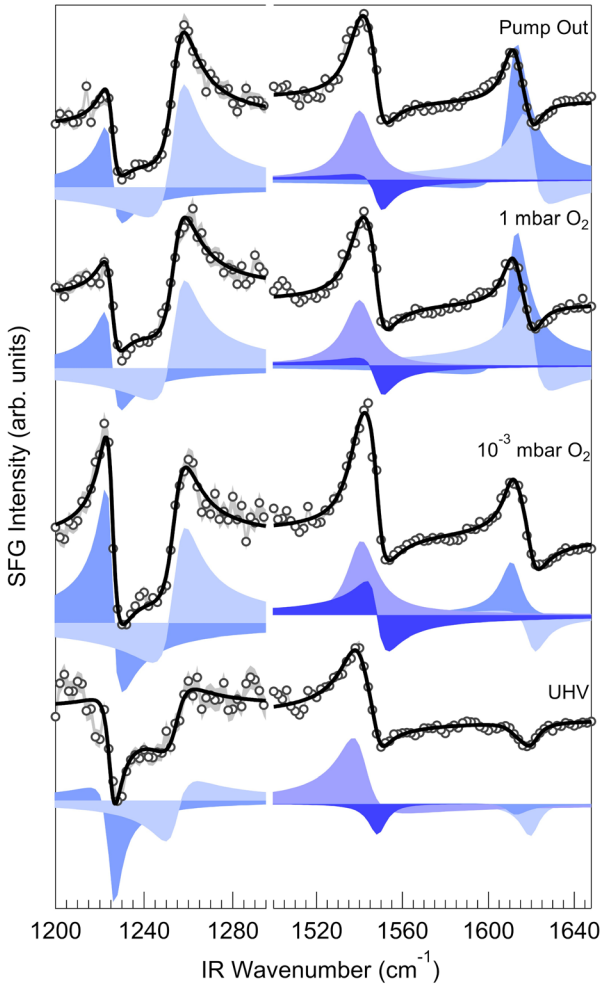

Fig. 7 Sum-frequency generation spectra of the pristine MnTPyP-Co layer (from bottom to top) in UHV, in near-ambient oxygen pressure (10^{-3} mbar and 1 mbar, respectively), and after recovering UHV conditions. All spectra were collected *in situ* and at room temperature with a visible laser wavelength of 532 nm in the ppp polarization combination.

Starting from the bottom row, the graph shows the spectrum of the pristine network in UHV, the measurements performed *in situ* at 1.5×10^{-3} and 1 mbar O_2 and the spectrum acquired after recovering vacuum conditions. Just as in the previous section, the spectra were modelled with two resonances in the low-energy range and four in the high-energy region, with globally fitted line positions and Lorentzian widths. The resulting best fit and decomposition profiles are shown in the figure. The resonant features evolve upon exposure to 1×10^{-3} mbar O_2 and further change when the background pressure is increased to 1 mbar.

Contrary to the low-pressure case, the pump out spectrum is identical to the one collected at the highest pressure, indicating no reversibility of the reaction (for a detailed, quantitative description refer to the SI of Table S1). We associate the non-reversible evolution with the accumulation and spillover of atomic oxygen. This confirms the activation of ligated molecular oxygen, leading to its splitting. Such a mechanism explains the different spectral evolution of a pristine sample when exposed to low or high oxygen pressure. Moreover, according to this interpretation, the evolution observed when the pressure is increased to 1 mbar can be justified by the further oxidation of the layer. It is reasonable to assume therefore that at such high pressure atomic oxygen might oxidize graphene or even intercalate below the sheet.[45,49] The modified network–graphene coupling within the heterostack would then affect the MnTPyP-Co properties, explaining the second spectral evolution step. We can prove that this is the case when looking at the corresponding core levels data (Fig. 8). When starting from the pristine layer in UHV and measuring *in situ* in 1×10^{-3} mbar O_2, four spectral contributions appear in the O 1s spectra (Fig. 8c). Two of those are found at 532.9 and 529.6 eV, respectively. The peaks observed at these energies at low pressure (Fig. 6c and Table S2), were associated with activated oxygen bonded to cobalt (Co–$O_2^{\delta-}$) and to atomic oxygen (Co–O), respectively. Contrary to the low O_2 pressure case, upon high O_2 pressure, more features can be clearly resolved at 530.8 and 532.0 eV. We ascribe them to distinct oxygen species formed on graphene. The former is close in energy to the feature already observed at low pressure, associated with enolate oxygen sitting on top of graphene.[46] The latter in turn could be attributed to ether groups, where an oxygen atom is embedded in the graphene lattice.[46] Upon oxygen pump out, the $O_2^{\delta-}$ peak is completely quenched, consistently with the low-pressure case. The amount of oxygen accumulated on the surface, relative to the low-pressure regime, can be roughly estimated by comparing the total areas of the O 1s signal, indicating that oxygen coverage is approximately 4 to 5 times higher in the high-pressure case. Due to the absence of O 1s features below 529 eV,[45,49] we assume that the amount of atomic O intercalated between Gr and Ir(111) is negligible. Moreover, the presence of intercalated oxygen normally causes the growth of two Ir $4f_{7/2}$ components chemically shifted by +0.3 and −0.2 eV with respect to the bulk peak at 60.8 eV,[49] which we do not observe (Fig. S4). The less pronounced minimum between the bulk and surface Ir $4f_{7/2}$ features is compatible with a weakly oxidized Gr/Ir(111).[45] Finally, the absence of a C 1s peak related to intercalated oxygen and expected at 283.6 eV (Fig. S4) further confirms the picture.[49] The new Co $2p_{3/2}$ components that emerge upon exposure to high oxygen background pressure (Fig. 8a) are challenging to interpret, particularly when compared to their low-pressure counterparts. The low energy peak at 779.4 eV is common to the low- and high-pressure spectra, while the high binding energy component is found now at 781.4 eV and the shoulder previously observed at 783.1 eV is not visible. The new peak at 779.4 eV could be ascribed to the GS feature of Co(II), related to Co–O or Co–$O_2^{\delta-}$ (Table S2). The discrepancy with the low-pressure case could possibly be explained by the oxygen-induced modified interaction between the MnTPyP-Co layer and graphene. Our hypothesis is consistent with the almost irreversible quenching of the Co(I) GS peak, suggesting the suppression of a charge-transfer channel as a consequence of

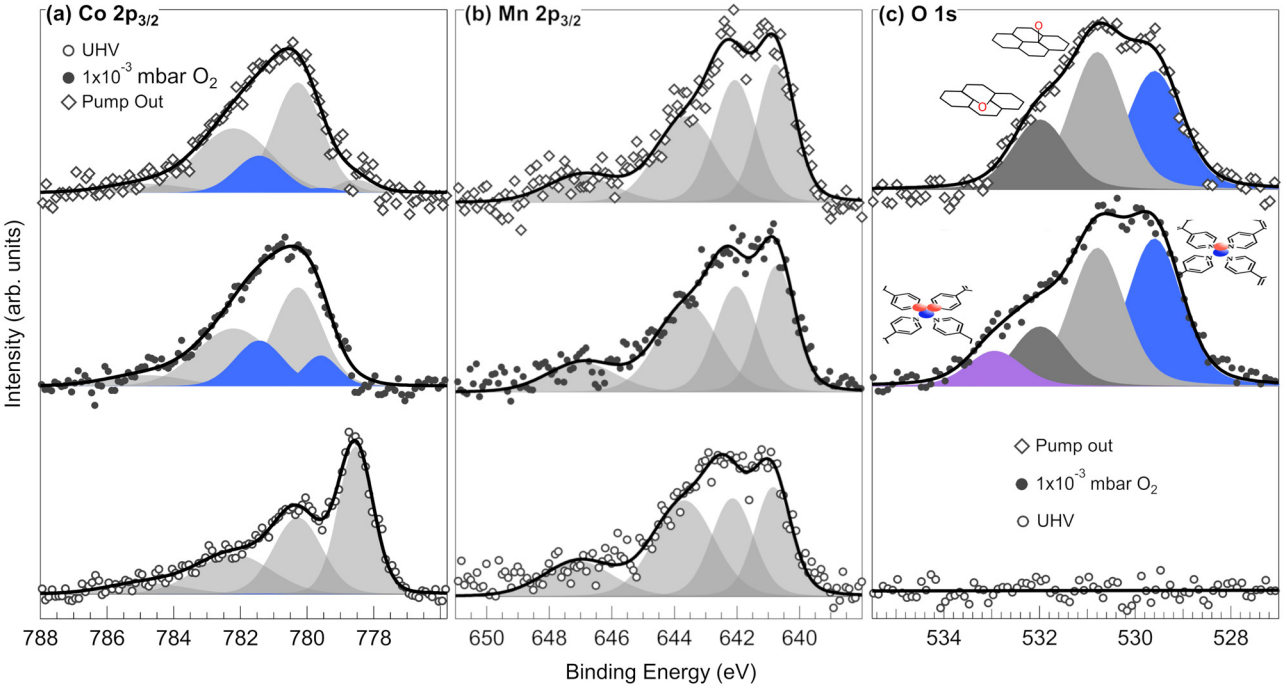

Fig. 8 XPS spectra of the pristine MnTPyP-Co layer in UHV (bottom), in near-ambient oxygen pressure (central row, 10^{-3} mbar), and after recovering UHV conditions (top row). (a) Co $2p_{3/2}$ and (b) Mn $2p_{3/2}$ core level regions were collected with a photon energy of 1000 eV, while for (c) the O 1s region photons of 750 eV were chosen for optimal measurement conditions.

the oxygen-enhanced decoupling from the support. However, this picture is extremely reductive, considering the co-presence of Co–O and Co–$O_2^{\delta-}$, and that the spectral line positions might also depend on the local amount of oxygen atoms spilling over on Gr in the proximity of the active metal sites. Contrary to Co, Mn seems to be almost unaffected by these processes (Fig. 8b), despite the partial graphene oxidation. The Mn $2p_{3/2}$ core level exhibits a minor shift upon exposure to O_2, probably induced by the oxidation of Co and Gr. The fit yields a non-reversible rigid shift of −130 meV of the Mn core level spectrum, where the first peak is displaced from 640.90 to 640.77 eV. The N 1s spectral evolution supports this picture (Fig. S4), with all features of the pristine layer shifting to lower binding energies in 1×10^{-3} mbar O_2, to the opposite side with respect to the N 1s shift upon Co coordination to the pristine monometallic MnTPyP layer. The macrocyclic nitrogen N 1s core level shifts by −0.3 eV, supporting the observed Mn $2p_{3/2}$ shift to lower binding energy. The pyridinic component is affected by a noticeable variation by −0.8 eV. Thus, both Mn $2p_{3/2}$ and N 1s core level spectra are drifting back towards the ones of a pristine MnTPyP layer. Such results suggest a partial oxygen-induced decoupling of Co from the molecules due to charge competition between N and O. Accordingly, the C 1s spectra display a shift of about −0.3 eV of the carbon components related to the network upon exposure to oxygen. Interestingly, the Gr peak is affected by a barely resolved energy displacement of about −50 meV. We would expect a shift towards higher binding energy, or the appearance of new peak shoulders growing at higher binding energy upon oxidation.[45] However, this behaviour is the result of a competition between the partial Gr oxidation and the influence of oxygen on the network–graphene interaction. Moreover, since the coverage of the Co active sites is of the order of 0.01 ML with respect to the graphene cell, this makes the O spillover minimal from a large-scale point of view.

We demonstrated that some of the effects of exposing the bi-metallic MOF to high oxygen background pressures are not reversible. For this reason, it is possible to oxidize the layer and perform the desired measurements also in an *ex situ* approach so to exploit UHV techniques. We collected the valence band spectra of the pristine MnTPyP-Co/Gr/Ir(111) in UHV, in 4×10^{-8} mbar O_2 and in UHV after a 30-minutes treatment in 5×10^{-6} mbar O_2 (Fig. S5). The pristine layer Energy Distribution Curve (EDC) shows two well-separated features, at 1.1 eV and 2.0 eV, associated to the HOMO and HOMO−1 of the MnTPyP-Co system, respectively. In low O_2 pressure, the HOMO−1 is barely affected. Instead, the HOMO shifts by +0.5 eV to 1.6 eV BE. Thus, we could say that the HOMO is the frontier orbital involved in the interaction and bonding of Co with oxygen, undergoing no further modification by exposure to higher oxygen pressure, while the HOMO−1 undergoes a minimal shift by −0.1 eV. Accordingly, the work function increases by 0.4 eV in low O_2 pressure and irreversibly shifts by 0.5 eV after exposure to higher pressure. The HOMO shift upon O_2 exposure is explained also within our DFT picture (Fig. S6). The projected density of states shows that in the pristine MnTPyP–Co/Gr, the HOMO is mainly constituted by Mn d_{xy} and $d_{x^2-y^2}$ and C p_{xy} orbitals. Upon O_2 adsorption, the

latter do not significantly take part in the Mn–O_2 interaction. Instead, the HOMO is shifted to lower energy due to the interaction between the Co d and O p orbitals (Fig. S7) for both the V- and H-configurations. We notice here that the measured and the calculated HOMO shifts agree only qualitatively. This is reasonable since in the experiment we also observe spillover of atomic O following dissociation at the metal sites, yielding the local oxidation of the graphene support. This latter phenomenon is known to induce some charge-doping of the metalorganic layer,[50] thus explaining the larger observed shift.

To confirm that the non-reversible modifications of the layer originate from the activation of the O_2 intramolecular bond and its consequent dissociation, we performed additional *in situ* SFG experiments in 1×10^{-3} mbar CO, in 1×10^{-3} mbar CO + 5×10^{-4} mbar O_2 (1.5×10^{-3} mbar in total, with a partial pressures ratio CO : O_2 = 2 : 1) and after recovering UHV (Fig. S8). The aim was to exploit the reducing capabilities of CO to attempt the removal of the atomic oxygen species originating from the O_2 decomposition, thus preventing the irreversible poisoning of graphene due to the accumulation of atomic oxygen. Exposure to 10^{-3} mbar CO leads to the growth of the expected C–O stretching resonances upon CO saturation of the Co(I) sites. The modes at 1948 and 1969 cm^{-1} are associated to the hot-band and fundamental vibrational excitations, respectively, in analogy to the CoTPyP-Co case.[23] Introduction of additional 5×10^{-4} mbar O_2, beyond the reversible oxidation regime, yields immediate quenching of the CO resonances, clearly showing that CO is destabilized and that competition for the same Co sites is taking place. Upon pumping out, the system shows good reversibility, recovering to a good approximation the pristine layer conditions and showing no evidence of oxidation. The close-to reversible evolution supports therefore CO oxidation and removal of atomic O yielding CO_2, preventing oxygen accumulation on the layer.

3 Conclusions

In summary, we have shown both computationally and experimentally that the single metal atom bimetallic layer that can be self-assembled on graphene by tetra-coordination of MnTPyP through Co adatoms shows interesting reactivity properties towards oxygen. In particular, while the Mn sites offer "end on", unstable coordination to the oxygen molecule, the Co(I) sites can coordinate both O atoms of the di-oxygen molecule in a horizontal bonding geometry. This is accompanied by charge transfer, intramolecular bond lengthening and a change in the Co oxidation state. The latter yields a triplet to singlet spin configuration transition and, consequently, di-oxygen activation in the form of a metastable superoxo species that can undergo dissociation. The process is pressure-dependent, where ligation is observed at equilibrium conditions at room temperature, while dissociation and progressive oxidation of the Co sites and of the underlying graphene support occur in the near-ambient pressure regime. The different behavior of the Mn and Co sites with respect to O_2 activation originates from the difference in the orbitals involved in the bonding hybridization process upon adsorption of the ligand. Mn d_{zx} and d_{zy} interaction with the oxygen $2p_z$ is found negligible due to the fact that these metal orbitals are already involved in strong covalent bonding with the four nitrogen atoms of the macrocycle (see Fig. S7 and the text in the SI for more details). Finally, by introducing a CO and O_2 gas mixture it is found that oxidation of the layer could be preserved *via* titration of the oxygen atoms generated by O_2 dissociation, yielding *de facto* a room temperature CO oxidation process viable.

4 Methods

4.1 Computational methods

Periodic spin-polarized density functional theory (DFT) calculations were carried out using the Quantum ESPRESSO package and a plane wave basis set.[51,52] The interaction between ions and valence electrons was accounted for using Vanderbilt's ultrasoft pseudopotentials.[53] Exchange–correlation effects were treated by using the Perdew–Burke–Ernzerhof (PBE) functional.[54] As semi-local functionals like PBE are insufficient to describe correlated Co 3d and Mn 3d electrons, Hubbard-type corrections (DFT+U) were incorporated.[55] The U values for both Mn and Co 3d were calculated using the self-consistent approach,[56] providing 3.2 and 6.1 eV for Mn and Co 3d electrons, respectively. Weak dispersive interactions were included by the non-local van der Waals dispersion corrections (DFT-DF3).[57] A kinetic energy cut-off of 60 Ry was used for plane waves (240 Ry for charge density). A Gaussian smearing with a 0.01 Ry width was used for Brillouin zone integration. The energy threshold for self-consistent minimization was set to 10^{-6} Ry, while the position relaxation was performed until the forces converged to 0.01 Ry $Bohr^{-1}$. The Brillouin zone sampling was performed using Γ-centred k-points on $2 \times 4 \times 1$ and $5 \times 10 \times 1$ grids, for relaxation and total energy calculation, respectively.

To compare experimental and DFT results, we considered two structural models, one for monometallic MnTPyP and one for bimetallic MnTPyP-Co with Mn occupying the core and Co at the peripheral sites, combined with a Gr layer. These two models are named MnTPyP/Gr and MnTPyP-Co/Gr hereafter. For MnTPyP/Gr, an oblique cell with lattice parameters a_1 = 30.97 Å, b_1 = 14.84 Å and α_1 = 63.8° was relaxed over an oblique Gr cell containing 78 hexagonal units, while MnTPyP-Co/Gr was described using a lattice with dimensions a_2 = 28.36 Å, b_2 = 20.23 Å and α_2 = 44.9° and 70 hexagonal units of graphene (Fig. 1a and b). The spurious interaction along the z-direction was minimized by adopting a cell height of ~20 Å, ensuring a vacuum of ~15 Å between the periodic images. The whole approach is fully consistent with our recent paper on the pristine system.[26] The adsorption energy E_{ads} of a single oxygen molecule was defined as

$$E_{ads} = E_{M/Gr+O_2} - (E_{M/Gr} + E_{O_2})$$

where $E_{M/Gr+O_2}$, $E_{M/Gr}$ and E_{O_2} are the DFT total energies of the combined system of O_2 adsorbed on the monometallic/bi-

metallic surface over Gr, of the pristine surfaces interacting with Gr and of the free O_2 molecule, respectively. The total energy of the O_2 molecule was determined using a cubic simulation cell with $a = b = c = 15$ Å. Reaction pathways and barriers were computed using the nudged elastic band (NEB) method. Electron density differences $\Delta n(r)$ were calculated by subtracting the individual charge densities of the adsorbates $n_{O_2}(r)$ and the pristine layers $n_{M/Gr}(r)$ from the combined system $n_{M/Gr+O_2}(r)$:

$$\Delta n(r) = n_{M/Gr+O_2} - (n_{M/Gr}(r) + n_{O_2}(r))$$

Positions were kept fixed with respect to $n_{M/Gr+O_2}$. The Bader charge analysis was performed to get a quantitative value of the charge density redistribution using the approach proposed in ref. 58. The d-band centres were evaluated as $\varepsilon_d = \frac{\int_{-\infty}^{E_F} E D_d(E) dE}{\int_{-\infty}^{E_F} D_d(E) dE}$, where $D_d(E)$ is the density of state projected on the d-states of the transition metal and E_F is the Fermi energy of the system.

4.2 Experimental methods

Sample preparation. The Ir(111) surface was cleaned by repeated cycles of Ar+ sputtering and annealing (2 keV, 1275–1375 K), alternated with exposure to 5×10^{-8} mbar O_2 at 300–1070 K to get rid of residual carbon contaminants. The single Gr/Ir(111) sheet was grown by C_2H_4 chemical vapor deposition (CVD) following established recipes adapted to the characteristics of each used setup: briefly, the clean sample was heated ($T > 1275$ K) and exposed to a C_2H_4 background (5×10^{-8} mbar) for 2 minutes. The gas pressure was then increased (up to 3×10^{-7} mbar), and finally the temperature was lowered while recovering ultra-high vacuum (UHV) conditions. Depending on the specific experimental setup, the quality of the Gr sheet was checked with LEED, XPS, or IR-Vis SFG. Mn(III) *meso*-tetra(4-pyridyl)porphyrin chloride molecules were purchased from Frontier Scientific. The molecules were outgassed at 470–525 K for several hours in a quartz or BN crucible in UHV to remove gas contaminants and organic residues. The Cl atom ligated to the central metal stabilizes the complex as Mn(III), and is thermally detached from the porphyrins when they are heated, resulting in a reduction of the metal centre to Mn(II).[26,59–63] Absence of Cl in the deposited layer was verified by XPS and STM.[26] The sublimation temperature was varied in the 650–680 K range according to the setup and the crucible-sample distance, achieving deposition rates of approximately 0.06 ML min^{-1}, in order to grow a full monolayer (ML) in about 15–20 minutes. The sample was kept at 473 K during the growth to promote ordering without affecting stability. The maximum achieved molecular surface coverage was kept below 1 ML to avoid kinetic hindrance in the reordering process upon Co post-coordination as well as the formation of a second layer. The bi-metallic heterostructure was obtained by physical vapor deposition (PVD) of Co atoms on the MnTPyP/Gr/Ir(111) layer, formed at the previous synthesis step. Deposition of Co was performed by resistively heating a Co wire (99.995% purity, 250 μm diameter) at the SFG Laboratory and HIPPIE beamline, and *via* electron bombardment of a Co rod at the AG Cinchetti Laboratory. In this manuscript, the Co coverage will be expressed referring to a porphyrin monolayer (ML), so that 1 ML Co corresponds to one Co adatom for each molecule in 1 ML MnTPyP, in analogy with our previous work on the CoTPyP-Co system.[21] In general, Co was dosed to achieve a Co to MnTPyP ratio lower than 1, to avoid formation of Co clusters due to excess Co.[21] The evaporation rates and the actual Co coverage were calibrated either by Auger electron spectroscopy (AES) or XPS, depending on the available method.

Sum-frequency generation spectroscopy. Infrared-Visible Sum-Frequency Generation (IR-Vis SFG)[64,65] vibronic spectroscopy measurements were performed in a dedicated setup at the Department of Physics of the University of Trieste, best described elsewhere.[66] Briefly, a UHV system with a base pressure of 5×10^{-11} mbar hosts standard surface science preparation and characterization techniques and is directly coupled with a high-pressure cell for *in situ* IR-Vis SFG spectroscopy. The laser beams enter and exit the cell through UHV-compatible BaF_2 windows. The excitation source (Ekspla, 1064 nm, 30 ps, 50 Hz) delivers a 532 nm (2.33 eV) visible beam, and tunable IR radiation in the 1000–4500 cm^{-1} range. The raw SFG spectra were normalized to the impinging infrared and visible excitation intensities, and to a reference signal from clean Au to account for the energy-dependent IR intensity and the time-dependent intensity fluctuations of the sources. The normalized SFG spectra were then analyzed by least-squares fitting to the widely adopted parametric, effective expression of the nonlinear second-order susceptibility.[64] Further details and examples can be found in our previous works.[24,50,66] In summary, by modeling the observed lineshapes, accounting for the resonant IR-Vis vibronic transitions and for the non-resonant background, we describe all the interference terms associated with the relative phases, and consider the Lorentzian broadening typical of a stimulated spectroscopic transition and related to the dephasing rate, which in turn stems from the excited-state lifetime and the elastic dephasing of the vibronic state.[67] In the figures, we plot the normalized IR-Vis SFG signal intensity (markers), together with the best fit (lines) and the resonances, each with its interference with the non-resonant background (color-filled profiles). The latter are calculated with the parameters obtained from the fitting procedure following the literature,[66] choosing one of the possible multiplet solutions associated with the non-unicity of the parameter sets.[68] In the present study, spectra were collected in both ppp and ssp (SFG-Vis-IR) light polarization combinations.

Ambient-pressure X-ray photoelectron spectroscopy. *In situ* and *operando* AP-XPS measurements at the surface–gas interface were performed at the HIPPIE beamline of the MAX IV synchrotron radiation facility in Lund.[69] A slow raster-scan of 0.5 μm s^{-1} was set up to prevent beam-induced degradation of the sample during the measurements. Mn and Co $2p_{3/2}$ core level spectra

were acquired upon excitation with 1000 eV photons, O 1s with 750 eV, N 1s with 514 eV, C 1s and Ir $4f_{7/2}$ with 400 eV photons, respectively, in order to optimize photoionization cross section and surface sensitivity. The binding energy scale was calibrated with respect to the bulk Ir $4f_{7/2}$ core level signal (60.87 eV) as a reference,[70] or with respect to the Fermi level. The XPS spectra were best fitted by least squares fitting methods according to the Doniach-Šunjić or Voigt lineshapes,[71] depending on the core level metallicity, after subtraction of a linear background or a polynomial function previously optimized on the clean sample reference background.

Valence band and work function spectroscopy. Ultra-violet Photoelectron Spectroscopy (UPS) data were acquired at room temperature using a KREIOS Photoemission Electron Microscope (PEEM-Specs GmbH).[72] The measurements were performed using a monochromatized UV helium lamp with the characteristic emission line at 21.2 eV. Beam damage effects were observed only after prolonged exposure, of the order of an hour, and then the sample was moved stepwise to measure on a fresh spot. The spectra were aligned by correcting the binding energy (BE) with the Fermi level, normalized and then the bare Gr/Ir(111) valence band (VB) spectrum was subtracted to remove the substrate contribution and have a clearer view of the molecular-related VB features. By measuring the secondary electron onset kinetic energy E_{onset} it is possible to extract the work function value according to $\phi = h\nu - (E_F - E_{onset})$, where E_F is the Fermi edge position (the same used to calibrate the energy scale) and $h\nu$ = 21.2 eV. The bias applied between sample and analyzer (10 kV) ensures collection of the whole photoelectron kinetic energy region of interest (±2 $Å^{-1}$).

Scanning tunnelling microscopy. The STM measurements were performed at the Microscopy labs of MAX IV Laboratory with a commercial VT UHV XA STM from Scienta-Omicron, GmbH, with electrochemically etched W tips purchased from Scienta-Omicron, GmbH. Imaging was performed at a sample temperature of ~110 K due to the otherwise high mobility of the molecules. The sign of the bias refers to the bias of the sample with respect to the tip.

Author contributions

E. V. conceived and designed the project. S. B., M. D. C., D. C., G. Z., A. N., N. V., and V. M. conducted the experiments. M. C. and G. Z. supervised the WF and VB measurements. M. S. provided fundamental assistance at the beamline. A. Y. performed the theoretical calculations, P. G. supervised them. A. Y. and E. V. discussed all results and edited the manuscript. All authors have reviewed and contributed to the published version of the manuscript.

Conflicts of interest

There are no conflicts to declare.

Data availability

Additional experimental and computational data supporting this article have been included as part of the supplementary information (SI). Supplementary information is available. See DOI: https://doi.org/10.1039/d5nr04824a.

Further data is available from the corresponding authors upon reasonable request.

Acknowledgements

This work was funded by Unione Europea – Next Generation EU through project PRIN2022 XXJNRS 2DOrNotToBe CUP J53D23001510006 and Next Generation EU, Missione 4 Componente 1 CUP J53D23016180001 PRIN PNRR P2022B3WCB 2Dgo3D. We acknowledge MAX IV Laboratory for time on beamline HIPPIE under proposals 20220031, 20220898 and 20221030. Research conducted at MAX IV, a Swedish national user facility, is supported by the Swedish Research Council under contract 2018-07152, the Swedish Governmental Agency for Innovation Systems under contract 2018-04969, and Formas under contract 2019-02496. A. Y. and P. G. acknowledge ISCRA for access to the LEONARDO supercomputer, owned by the EuroHPC Joint Undertaking, hosted by CINECA (Italy). V. M., G. Z. and M. C. acknowledge funding from the DFG (Major Research Instrumentation Individual Proposal INST 212/409-1), and by "the Ministerium für Kultur und Wissenschaft des Landes Nordrhein-Westfalen (NRW)".

References

1 D. Dolphin and R. H. Felton, *Acc. Chem. Res.*, 1974, **7**, 26–32.
2 C. Rubio-Verdú, A. Sarasola, D.-J. Choi, Z. Majzik, R. Ebeling, M. R. Calvo, M. M. Ugeda, A. Garcia-Lekue, D. Sánchez-Portal and J. I. Pascual, *Commun. Phys.*, 2018, **1**, 15.
3 Z. Wang, S. Yuan, A. Mason, B. Reprogle, D.-J. Liu and L. Yu, *Macromolecules*, 2012, **45**, 7413–7419.
4 K. Biswas, M. Urbani, A. Sánchez-Grande, D. Soler-Polo, K. Lauwaet, A. Matěj, P. Mutombo, L. Veis, J. Brabec, K. Pernal, J. M. Gallego, R. Miranda, D. Écija, P. Jelínek, T. Torres and J. I. Urgel, *J. Am. Chem. Soc.*, 2022, **144**, 12725–12731.
5 T. Smok, S. Shakouri, E. Abouzari-Lotf, F. Pammer, T. Diemant, S. Jana, A. Roy, Y. Xiu, S. Klyatskaya, M. Ruben, Z. Zhao-Karger and M. Fichtner, *Batteries Supercaps*, 2023, **6**, e202300308.
6 W. Zhang, W. Lai and R. Cao, *Chem. Rev.*, 2017, **117**, 3717–3797.
7 M. Stredansky, S. Moro, M. Corva, H. Sturmeit, V. Mischke, D. Janas, I. Cojocariu, M. Jugovac, A. Cossaro, A. Verdini, L. Floreano, Z. Feng, A. Sala, G. Comelli, A. Windischbacher, P. Puschnig, C. Hohner, M. Kettner, J. Libuda, M. Cinchetti, C. M. Schneider, V. Feyer, E. Vesselli and G. Zamborlini, *Angew. Chem., Int. Ed.*, 2022, **61**, e202201916.

8 H. M. Sturmeit, I. Cojocariu, A. Windischbacher, P. Puschnig, C. Piamonteze, M. Jugovac, A. Sala, C. Africh, G. Comelli, A. Cossaro, A. Verdini, L. Floreano, M. Stredansky, E. Vesselli, C. Hohner, M. Kettner, J. Libuda, C. M. Schneider, G. Zamborlini, M. Cinchetti and V. Feyer, *Small*, 2021, **17**, 2104779.
9 S. Ovalle and C. Malardier-Jugroot, *J. Comput. Chem.*, 2025, **46**, e27505.
10 W. Hieringer, K. Flechtner, A. Kretschmann, K. Seufert, W. Auwärter, J. V. Barth, A. Görling, H.-P. Steinrück and J. M. Gottfried, *J. Am. Chem. Soc.*, 2011, **133**, 6206–6222.
11 J. M. Gottfried, *Surf. Sci. Rep.*, 2015, **70**, 259–379.
12 W. Auwärter, D. Écija, F. Klappenberger and J. V. Barth, *Nat. Chem.*, 2015, **7**, 105–120.
13 X. M. Hu, M. H. Rønne, S. U. Pedersen, T. Skrydstrup and K. Daasbjerg, *Angew. Chem., Int. Ed.*, 2017, **56**, 6468–6472.
14 P. K. Sonkar, K. Prakash, M. Yadav, V. Ganesan, M. Sankar, R. Gupta and D. K. Yadav, *J. Mater. Chem. A*, 2017, **5**, 6263–6276.
15 B. Wurster, D. Grumelli, D. Hötger, R. Gutzler and K. Kern, *J. Am. Chem. Soc.*, 2016, **138**, 3623–3626.
16 I. Azcarate, C. Costentin, M. Robert and J. M. Savéant, *J. Am. Chem. Soc.*, 2016, **138**, 16639–16644.
17 M. Bevilacqua, J. Filippi, A. Lavacchi, A. Marchionni, H. A. Miller, W. Oberhauser, E. Vesselli and F. Vizza, *Energy Technol.*, 2014, **2**, 522–525.
18 Y. Li, J. Xiao, T. E. Shubina, M. Chen, Z. Shi, M. Schmid, H.-P. Steinrück, J. M. Gottfried and N. Lin, *J. Am. Chem. Soc.*, 2012, **134**, 6401–6408.
19 D. Hötger, M. Etzkorn, C. Morchutt, B. Wurster, J. Dreiser, S. Stepanow, D. Grumelli, R. Gutzler and K. Kern, *Phys. Chem. Chem. Phys.*, 2019, **21**, 2587–2594.
20 B. Mandal, J. S. Chung and S. G. Kang, *J. Phys. Chem. C*, 2018, **122**, 9899–9908.
21 F. Armillotta, D. Bidoggia, S. Baronio, A. Sala, R. Costantini, M. dell'Angela, I. Cojocariu, V. Feyer, A. Morgante, M. Peressi and E. Vesselli, *Adv. Funct. Mater.*, 2024, **34**, 2408200.
22 D. Bidoggia, F. Armillotta, A. Sala, E. Vesselli and M. Peressi, *J. Phys. Chem. C*, 2024, **128**, 1737–1745.
23 F. Armillotta, A. Sala and E. Vesselli, *J. Phys. Chem. C*, 2024, **128**, 15613–15623.
24 F. Armillotta, D. Bidoggia, S. Baronio, P. Biasin, A. Annese, M. Scardamaglia, S. Zhu, B. Bozzini, S. Modesti, M. Peressi and E. Vesselli, *ACS Catal.*, 2022, 7950–7959.
25 F. Armillotta, A. Pividori, M. Stredansky, N. Seriani and E. Vesselli, *Top. Catal.*, 2020, **63**, 1585–1595.
26 S. Baronio, M. De Col, A. Yadav, B. Roondhe, V. Mischke, O. Resel, D. Bidoggia, A. Namar, N. Vinogradov, M. Scardamaglia, M. Valvidares, P. Gargiani, M. Cinchetti, G. Zamborlini, P. Giannozzi and E. Vesselli, *Nanoscale*, 2025, **17**, 16946–16963.
27 D. Rutkowska-Zbik, R. Tokarz-Sobieraj and M. Witko, *J. Chem. Theory Comput.*, 2007, **3**, 914–920.
28 J. Conradie and A. Ghosh, *J. Phys. Chem. B*, 2016, **120**, 4972–4979.
29 R. B. Araujo, G. L. S. Rodrigues, E. C. Dos Santos and L. G. M. Pettersson, *Nat. Commun.*, 2022, **13**, 6853.
30 H.-R. Liu, H. Xiang and X. G. Gong, *J. Chem. Phys.*, 2011, **135**, 214702.
31 K. P. Kepp, *Coord. Chem. Rev.*, 2017, **344**, 363–374.
32 M. E. Ali, B. Sanyal and P. M. Oppeneer, *J. Phys. Chem. B*, 2012, **116**, 5849–5859.
33 M. Tsuda, E. Sy Dy and H. Kasai, *J. Chem. Phys.*, 2005, **122**, 244719.
34 D. D. Miller, R. Siriwardane and T. Simonyi, *Energy Fuels*, 2011, **25**, 4261–4270.
35 M. Corva, A. Ferrari, M. Rinaldi, Z. Feng, M. Roiaz, C. Rameshan, G. Rupprechter, R. Costantini, M. Dell'Angela, G. Pastore, G. Comelli, N. Seriani and E. Vesselli, *Nat. Commun.*, 2018, **9**, 4703.
36 M. Kozuka and K. Nakamoto, *J. Am. Chem. Soc.*, 1981, **103**, 2162–2168.
37 D. Den Boer, M. Li, T. Habets, P. Iavicoli, A. E. Rowan, R. J. M. Nolte, S. Speller, D. B. Amabilino, S. De Feyter and J. A. A. W. Elemans, *Nat. Chem.*, 2013, **5**, 621–627.
38 O. Gunnarsson and K. Schönhammer, *Phys. Rev. Lett.*, 1978, **41**, 1608–1612.
39 M. C. Biesinger, B. P. Payne, A. P. Grosvenor, L. W. M. Lau, A. R. Gerson and R. S. C. Smart, *Appl. Surf. Sci.*, 2011, **257**, 2717–2730.
40 F. Armillotta, D. Bidoggia, P. Biasin, A. Annese, A. Cossaro, A. Verdini, L. Floreano, M. Peressi and E. Vesselli, *Cell Rep. Phys. Sci.*, 2023, 101378.
41 I. Cojocariu, S. Carlotto, G. Zamborlini, M. Jugovac, L. Schio, L. Floreano, M. Casarin, V. Feyer and C. M. Schneider, *J. Mater. Chem. C*, 2021, **9**, 12559–12565.
42 C. Puglia, A. Nilsson, B. Hernnäs, O. Karis, P. Bennich and N. Mårtensson, *Surf. Sci.*, 1995, **342**, 119–133.
43 C. T. Campbell, *Surf. Sci.*, 1986, **173**, L641–L646.
44 B. Bozzini, A. Previdi, M. Amati, M. Bevilacqua, G. Cordaro, M. Corva, A. Donazzi, G. Dotelli, L. Gregoratti, R. Pelosato, M. Vorokhta and E. Vesselli, *J. Power Sources*, 2019, **436**, 226815.
45 N. A. Vinogradov, K. Schulte, M. L. Ng, A. Mikkelsen, E. Lundgren, N. Mårtensson and A. B. Preobrajenski, *J. Phys. Chem. C*, 2011, **115**, 9568–9577.
46 S. Kyrkjebø, A. Cassidy, N. Akhtar, R. Balog, M. Scheffler, L. Hornekær, B. Holst and R. Flatabø, *Carbon*, 2021, **174**, 396–403.
47 J. Haber, J. Stoch and L. Ungier, *J. Electron Spectrosc. Relat. Phenom.*, 1976, **9**, 459–467.
48 R. E. Berry, *Comprehensive Coordination Chemistry II*, Elsevier, 2003, pp. 625–629.
49 E. Grånäs, J. Knudsen, U. a. Schröder, T. Gerber, C. Busse, M. a. Arman, K. Schulte, J. N. Andersen and T. Michely, *ACS Nano*, 2012, **6**, 9951–9963.
50 M. Corva, F. Mohamed, E. Tomsic, M. Rinaldi, C. Cepek, N. Seriani, M. Peressi and E. Vesselli, *J. Phys. Chem. C*, 2019, **123**, 3916–3922.
51 P. Giannozzi, S. Baroni, N. Bonini, M. Calandra, R. Car, C. Cavazzoni, D. Ceresoli, G. L. Chiarotti, M. Cococcioni,

I. Dabo, A. Dal Corso, S. de Gironcoli, S. Fabris, G. Fratesi, R. Gebauer, U. Gerstmann, C. Gougoussis, A. Kokalj, M. Lazzeri, L. Martin-Samos, N. Marzari, F. Mauri, R. Mazzarello, S. Paolini, A. Pasquarello, L. Paulatto, C. Sbraccia, S. Scandolo, G. Sclauzero, A. P. Seitsonen, A. Smogunov, P. Umari and R. M. Wentzcovitch, *J. Phys.: Condens. Matter*, 2009, **21**, 395502.

52 P. Giannozzi, O. Andreussi, T. Brumme, O. Bunau, M. Buongiorno Nardelli, M. Calandra, R. Car, C. Cavazzoni, D. Ceresoli, M. Cococcioni, N. Colonna, I. Carnimeo, A. Dal Corso, S. de Gironcoli, P. Delugas, R. A. DiStasio, A. Ferretti, A. Floris, G. Fratesi, G. Fugallo, R. Gebauer, U. Gerstmann, F. Giustino, T. Gorni, J. Jia, M. Kawamura, H.-Y. Ko, A. Kokalj, E. Küçükbenli, M. Lazzeri, M. Marsili, N. Marzari, F. Mauri, N. L. Nguyen, H.-V. Nguyen, A. Otero-de-la-Roza, L. Paulatto, S. Poncé, D. Rocca, R. Sabatini, B. Santra, M. Schlipf, A. P. Seitsonen, A. Smogunov, I. Timrov, T. Thonhauser, P. Umari, N. Vast, X. Wu and S. Baroni, *J. Phys.: Condens. Matter*, 2017, **29**, 465901.

53 K. F. Garrity, J. W. Bennett, K. M. Rabe and D. Vanderbilt, *Comput. Mater. Sci.*, 2014, **81**, 446–452.

54 J. P. Perdew, K. Burke and M. Ernzerhof, *Phys. Rev. Lett.*, 1996, **77**, 3865–3868.

55 M. Cococcioni and S. de Gironcoli, *Phys. Rev. B: Condens. Matter Mater. Phys.*, 2005, **71**, 035105.

56 I. Timrov, N. Marzari and M. Cococcioni, *Comput. Phys. Commun.*, 2022, **279**, 108455.

57 S. Grimme, J. Antony, S. Ehrlich and H. Krieg, *J. Chem. Phys.*, 2010, **132**, 154104.

58 G. Henkelman, A. Arnaldsson and H. Jónsson, *Comput. Mater. Sci.*, 2006, **36**, 354–360.

59 J. P. Beggan, S. A. Krasnikov, N. N. Sergeeva, M. O. Senge and A. A. Cafolla, *Nanotechnology*, 2012, **23**, 235606.

60 S. R. Alharbi, A. A. A. Darwish, S. E. A. Garni, H. I. ElSaeedy and K. F. A. El-Rahman, *Infrared Phys. Technol.*, 2016, **78**, 77–83.

61 A. A. Attia, A. M. A. El-Barry, E. A. A. El-Shazly and L. M. D. El-Deen, *J. Lumin.*, 2018, **199**, 391–399.

62 B. E. Murphy, S. A. Krasnikov, N. N. Sergeeva, A. A. Cafolla, A. B. Preobrajenski, A. N. Chaika, O. Lübben and I. V. Shvets, *ACS Nano*, 2014, **8**, 5190–5198.

63 G. Kyriakou, M. B. Boucher, A. D. Jewell, E. A. Lewis, T. J. Lawton, A. E. Baber, H. L. Tierney, M. Flytzani-Stephanopoulos and E. C. H. Sykes, *Science*, 2012, **335**, 1209–1212.

64 C. S. Tian and Y. R. Shen, *Surf. Sci. Rep.*, 2014, **69**, 105–131.

65 Y. R. Shen, *Nature*, 1989, **337**, 519–525.

66 M. Corva, Z. Feng, C. Dri, F. Salvador, P. Bertoch, G. Comelli and E. Vesselli, *Phys. Chem. Chem. Phys.*, 2016, **18**, 6763–6772.

67 M. Bonn, C. Hess, W. G. Roeterdink, H. Ueba and M. Wolf, *Chem. Phys. Lett.*, 2004, **388**, 269–273.

68 B. Busson and A. Tadjeddine, *J. Phys. Chem. C*, 2009, **113**, 21895–21902.

69 S. Zhu, M. Scardamaglia, J. Kundsen, R. Sankari, H. Tarawneh, R. Temperton, L. Pickworth, F. Cavalca, C. Wang, H. Tissot, J. Weissenrieder, B. Hagman, J. Gustafson, S. Kaya, F. Lindgren, I. Källquist, J. Maibach, M. Hahlin, V. Boix, T. Gallo, F. Rehman, G. D'Acunto, J. Schnadt and A. Shavorskiy, *J. Synchrotron Radiat.*, 2021, **28**, 624–636.

70 M. Bianchi, D. Cassese, A. Cavallin, R. Comin, F. Orlando, L. Postregna, E. Golfetto, S. Lizzit and A. Baraldi, *New J. Phys.*, 2009, **11**, 063002.

71 S. Doniach and M. Sunjic, *J. Phys. C: Solid State Phys.*, 1970, **3**, 285–291.

72 D. M. Janas, A. Windischbacher, M. S. Arndt, M. Gutnikov, L. Sternemann, D. Gutnikov, T. Willershausen, J. E. Nitschke, K. Schiller, D. Baranowski, V. Feyer, I. Cojocariu, K. Dave, P. Puschnig, M. Stupar, S. Ponzoni, M. Cinchetti and G. Zamborlini, *Inorg. Chim. Acta*, 2023, **557**, 121705.